RESEARCH ARTICLE

National Science Review
8: nwaa191, 2021
https://doi.org/10.1093/nsr/nwaa191
Advance access publication 29 August 2020

MATERIALS SCIENCE

Diatom-inspired multiscale mineralization of patterned protein–polysaccharide complex structures

Ke Li[1,†], Yingfeng Li[1,†], Xinyu Wang[1], Mengkui Cui[1], Bolin An[1], Jiahua Pu[1], Jintao Liu[1], Boyang Zhang[1], Guijun Ma[1] and Chao Zhong[1,2,3,*]

ABSTRACT

Marine diatoms construct their hierarchically ordered, three-dimensional (3D) external structures called frustules through precise biomineralization processes. Recapitulating the remarkable architectures and functions of diatom frustules in artificial materials is a major challenge that has important technological implications for hierarchically ordered composites. Here, we report the construction of highly ordered, mineralized composites based on fabrication of complex self-supporting porous structures—made of genetically engineered amyloid fusion proteins and the natural polysaccharide chitin—and performing *in situ* multiscale protein-mediated mineralization with diverse inorganic materials, including SiO_2, TiO_2 and Ga_2O_3. Subsequently, using sugar cubes as templates, we demonstrate that 3D fabricated porous structures can become colonized by engineered bacteria and can be functionalized with highly photoreactive minerals, thereby enabling co-localization of the photocatalytic units with a bacteria-based hydrogenase reaction for a successful semi-solid artificial photosynthesis system for hydrogen evolution. Our study thus highlights the power of coupling genetically engineered proteins and polysaccharides with biofabrication techniques to generate hierarchically organized mineralized porous structures inspired by nature.

Keywords: biomimetic mineralization, patterned porous structure, genetic engineering, amyloid protein, artificial photosynthesis

[1]School of Physical Science and Technology, ShanghaiTech University, Shanghai 201210, China; [2]Center for Materials Synthetic Biology, Shenzhen Institute of Synthetic Biology, Shenzhen Institutes of Advanced Technology, Chinese Academy of Sciences, Shenzhen 518055, China and [3]CAS Key Laboratory of Quantitative Engineering Biology, Shenzhen Institute of Synthetic Biology, Shenzhen Institutes of Advanced Technology, Chinese Academy of Sciences, Shenzhen 518055, China

*Corresponding authors. E-mails: zhongchao@shanghaitech.edu.cn; chao.zhong@siat.ac.cn
†Equally contributed to this work.

Received 20 March 2020; **Revised** 27 July 2020; **Accepted** 2 August 2020

INTRODUCTION

Biological organisms such as diatoms, sponges and radiolarians are able to make hierarchically organized, mineralized structures across multiple length scales [1–3]. One particularly interesting example is diatoms—unicellular, eukaryotic algae—which are well known to produce a wide variety of hierarchically ordered porous silica structures in a genetically controlled manner [1–4]. The diatom frustule (i.e. the hard and porous external layer of diatoms) is multifunctional: it serves as a protective barrier between the cytoplasm and the exterior environment, and it also provides mechanical strength to predation [3,4]. Furthermore, the micro-scale, periodic structure of the frustule possesses interesting light-directing properties, which diatoms are known to exploit to enhance their photosynthetic capacity [5–7]. Accordingly, diatoms have long served as a fruitful source of inspiration for fabrication of novel bio-inspired hierarchically porous materials.

Over several decades, numerous strategies have been used for *in vitro* generation of nanostructured silica-based material structures, including, for example, use of organic molecules (such as surfactants, polymers and organo-gelators) to guide silica mineral formation [8–13]. Most organic templates used in these efforts have been based on long-chain cationic polymers, mainly polyamines, to mimic the positively charged sequences of the silaffin proteins known to orchestrate diatom frustule biogenesis [14–19]. These organic templates can control the size and morphology of the silica particles that form; however, to date, these strategies have yielded relatively simple shapes such as rods, spheres or hexagonal platelets [14,20–23]. Other research efforts have focused on application of various three-dimensional assemblies of organic matrices (cellulose, collagen and virus) for structured aggregation of silica particles to form higher-order silica structures [14,15,24–30]. These *in vitro*

© The Author(s) 2020. Published by Oxford University Press on behalf of China Science Publishing & Media Ltd. This is an Open Access article distributed under the terms of the Creative Commons Attribution License (http://creativecommons.org/licenses/by/4.0/), which permits unrestricted reuse, distribution, and reproduction in any medium, provided the original work is properly cited.

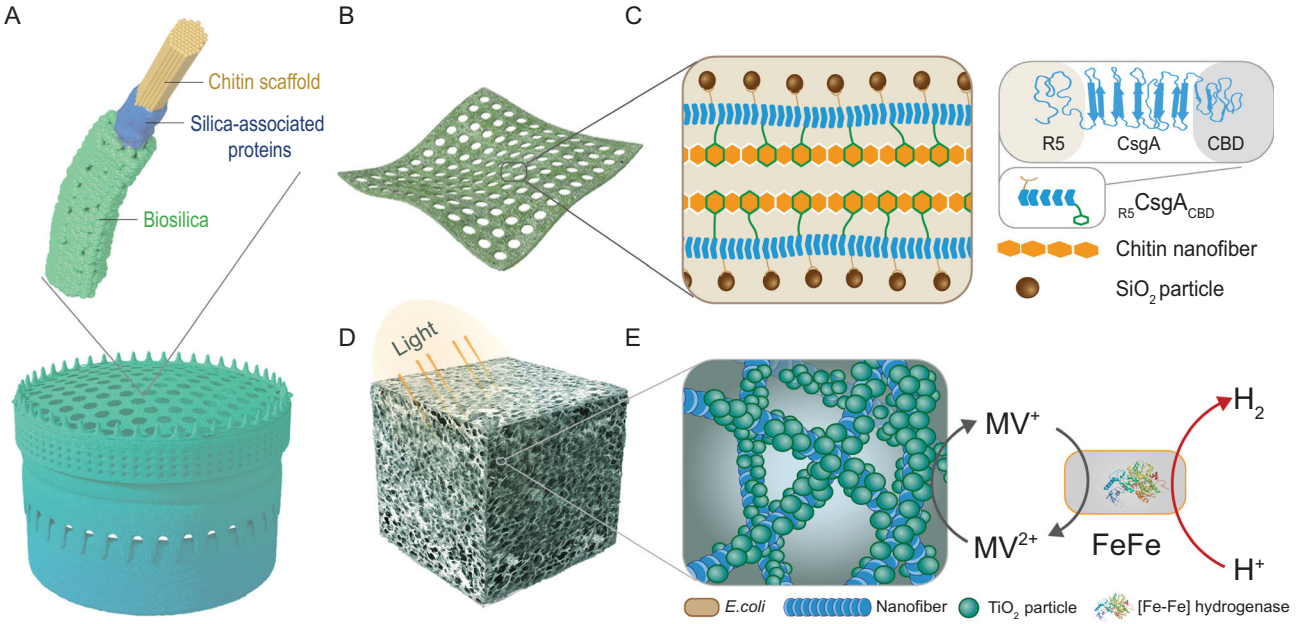

Figure 1. Bio-inspired construction of self-supporting porous structures using engineered multifunction amyloid fusion proteins as scaffolds for *in situ* mineralization. (A) Schematic of a typical diatom ordered porous structure comprising a chitin scaffold, silica-associated proteins and biosilica. (B and C) Schematic of the components of self-supporting patterned porous sheets (PPS) obtained by engineering strong amyloid/chitin interactions within the nanofiber matrix. (D and E) Schematic illustration of an artificial photosynthesis system for H_2 evolution based on 3D mineralized $_{R5}CsgA_{CBD}$/chitin cubes.

scaffolds have led to controlled deposition and organization of silica and some metal oxide minerals [31–33]. Additionally, diatom frustule-inspired scaffolds such as DNA origami architectures and micro-patterned functional silk structures have been explored to produce spatially ordered, nano- or micro-sized mineralized composites [34,35]. Despite important advances in biomimetic mineralization research, the development of mineralized structures recapitulating the hierarchically ordered porous structures of diatoms across multiple length scales remains elusive.

Here, aiming to recapitulate the hierarchically porous mineral structures and functional properties of diatom frustules (Fig. 1A), we developed a biomimetic mineralization strategy in which complex porous structures made of genetically engineered multifunctional amyloid fusion proteins and the polysaccharide chitin are used as scaffolds for *in situ* mineralization of both SiO_2 and metal oxides across multiple length scales. Our design was inspired by biogenesis of mineralized frustule structures. First, a three-domain fusion protein was engineered to comprise the CsgA protein from the well-known curli amyloid system of *Escherichia coli* (*E. coli*) [36,37], a chitin binding domain (CBD) from *Bacillus circulans* [38] and the R5 silica-nucleation peptide from *Clavulinopsis fusiformis* [24,39–41]. This design aimed to mimic the molecular interactions intrinsic to natural diatom systems in which chitin-based networks serve as a framework for silica mineralization during frustule formation, while soluble biomolecules such as silaffins are then used as silica-nucleating proteins to promote mineralization within the chitin matrix [39–42]. Second, two types of porous structures were produced to morphologically resemble the porous features of the diatom frustule, including a highly ordered 2D porous sheet fabricated via replica molding and a 3D irregular porous cube created using sugar cube as a template (Fig. 1B and D).

Using a biomimetic mineralization strategy, the 2D patterned and 3D irregular porous self-supporting protein/chitin composite structures can further template the formation of complex mineral architectures across multiple length scales (from nm to cm) (Fig. 1C and E). Extending the application of these multiscale mineralized structures, we demonstrate a hybrid artificial photosynthesis system based on a sugar-cube templated, 3D, biocompatible structure mineralized with photoreactive TiO_2 and colonized with hydrogenase-expressing bacteria for successful hydrogen production (Fig. 1E).

RESULTS

Bio-inspired construction of silicified self-supporting porous $_{R5}CsgA_{CBD}$/chitin sheets

To mimic the multiscale mineralization of diatom frustules, we started by rationally designing

self-assembling nanofiber networks capable of both promoting local silica nucleation and mineralization at the molecular level and recapturing protein–polysaccharide interactions that occur in diatom frustules. Specifically, we initially constructed and tested mineralization-promoting CsgA fusion proteins by genetically appending a SiO_2-nucleation peptide (R5) at the N-terminus of CsgA ($_{R5}$CsgA), a bacterial structural amyloid protein of *E. coli* biofilms that is amenable for genetic modification to endow functional properties without disrupting its nanofiber self-assembly capability [37,43]. We confirmed that the $_{R5}$CsgA fusion proteins could self-assemble into amyloid nanofibers (Supplementary Fig. 1) and found that they could indeed serve as a template for promoting silica formation (Supplementary Fig. 2). To engineer protein–polysaccharide molecular interactions, we designed CsgA fusion proteins containing CBD at C-terminus ($CsgA_{CBD}$). For context, the $CsgA_{CBD}$ fusion proteins had previously been demonstrated by our research group to enable strong and specific protein–chitin molecular interactions, resulting in networked chitin–amyloid nanofiber soft hybrid materials [37].

Our final functional protein module was therefore settled on engineered multidomain amyloid fusion proteins ($_{R5}CsgA_{CBD}$) in which the R5 peptide and CBD were genetically fused at the N- and C-termini of CsgA, respectively (Supplementary Figs 3 and 4). Morphological characterization by atomic force microscopy (AFM) and transmission electronic microscopy (TEM) revealed that the $_{R5}CsgA_{CBD}$ fusion proteins in solution could self-assemble into nanofibers, with an average fiber diameter of 1.7 ± 0.4 nm and an average length of 1097.5 ± 181.0 nm (Fig. 2A, B and Supplementary Fig. 5). Further, structural characterization by X-ray fiber diffraction revealed that the nanofibers displayed a typical β diffraction pattern, with a meridional reflection (denoted as d_2 in the diffraction pattern) at 4.8 Å, reflecting the spacing between β-strands within each layer of β-sheets and an equatorial reflection (denoted as d_1 in the diffraction patterns) at 9.5 Å, corresponding to inter-sheet packing distances (Fig. 2C) [43].

We then tested the self-assembling nanofibers composed of $_{R5}CsgA_{CBD}$ fusion proteins as organic templates for silica formation. After 10-min incubation in a precursor solution of tetramethoxysilane (TEOS) at room temperature, spherical SiO_2 particles were found to appear around the nanofibers, clearly suggesting that the nucleation process of SiO_2 was guided by the nanofibers (Fig. 2D, left). In contrast, other CsgA fusion proteins that do not contain R5 domain seemed not to promote the deposition of SiO_2 nanoparticles under the same silicification conditions (Supplementary Fig. 6). In addition, a series of chemical mapping analyses using an energy dispersive spectrometer (EDS) coupled with electron microscopy imaging confirmed the silica mineralization of the amyloid fibers comprising the $_{R5}CsgA_{CBD}$ fusion monomers (Fig. 2D, right).

We next designed self-supporting porous structures consisting of $_{R5}CsgA_{CBD}$/chitin complex components for multiscale silica mineralization, largely inspired from the porous structure of the diatom frustule. Using a simple microtransfer molding process, we fabricated complex self-supporting structures made of $_{R5}$CsgA proteins and the polysaccharide chitin (Fig. 2E and G) [44]. Through a methanol-assisted *in situ* curing process, CsgA fusion proteins in the fabricated structures would regain their amyloid β-sheet structures with fibrous morphology [37]. Briefly, using an hexafluoroisopropanol (HFIP) solution containing both the engineered $_{R5}CsgA_{CBD}$ protein monomers and dissolved squid pen β-chitin molecules, we printed and cured structures that we term patterned porous sheets (PPS) (Fig. 2E). Upon methanol vapor exposure, the protein monomers in the fabricated complex structures indeed reassembled into their characteristic nanofiber structures (Fig. 2G and I). In addition, the PPS composed of chitin and $_{R5}CsgA_{CBD}$ fusion proteins (length, ∼1 cm; width, ∼1 cm; thickness, 412 ± 15 nm and pore diameter, ∼10 μm) exhibited impressive durability and stability after exposure to aqueous solution, in sharp contrast to the deterioration we observed for incomplete PPS structures built solely of $_{R5}CsgA_{CBD}$ fusion proteins (i.e. lacking the polysaccharide chitin) (Supplementary Fig. 7). When these patterned porous sheets were exposed to a mineralization precursor solution of tetramethoxysilane for *in situ* mineralization (Fig. 2F), silica spheres appeared to form on the PPS surface, as revealed by AFM and scanning electron microscopy (SEM) (Fig. 2H and J). In contrast, deposition of silica spheres was not clearly found on the pure chitin PPS sheets, highlighting the role of fusion proteins in promoting silica formation (Supplementary Fig. 8). In addition, silica deposition was found to occur preferably at neutral pH (7.5), rather than at basic (10.5) or acidic (4.5) pH value (Supplementary Fig. 9), in agreement with phenomena reported in previously published works [24,45]. Examination of the mineralized structures by X-ray photoelectron spectroscopy (XPS) confirmed successful PPS silicification: these mineralized PPS exhibited characteristic binding energies of 146 eV and 102 eV for electrons found in the 2s and 2p electron shells of the silicon atom, respectively (Fig. 2K). Further characterization by Fourier Transform Infrared

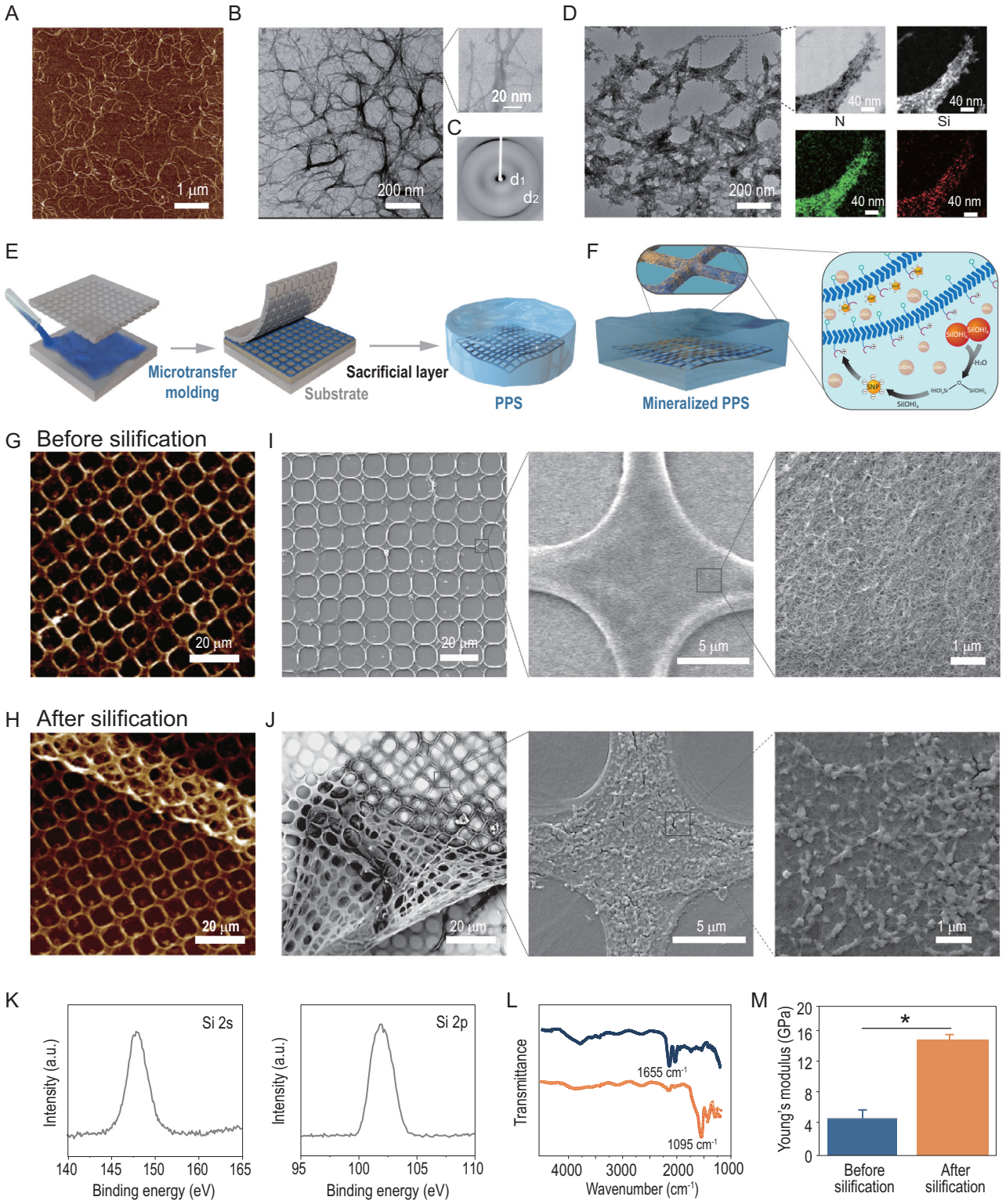

Figure 2. Morphologies, structural characterization and mechanical properties of rationally designed self-assembling $_{R5}CsgA_{CBD}$ nanofibers, self-supporting PPS and their corresponding mineralized architectures. (A–C) Morphological and structural characterization of the native amyloid nanofibers which self-assemble from the $_{R5}CsgA_{CBD}$ fusion proteins: (A) AFM image, (B) TEM images and (C) X-ray fiber diffraction pattern. (D) TEM images and STEM-EDS of the silicified $_{R5}CsgA_{CBD}$ nanofibers. (E) Schematic showing the bio-inspired construction of self-supporting PPS by coupling microtransfer molding with HFIP ink composed of dissolved $_{R5}CsgA_{CBD}$ monomers and squid pen polysaccharide β-chitin. (F) Schematic showing biomimetic mineralization of PPS in the presence of TEOS solution to produce silicified PPS. (G, H) AFM images of non-mineralized (G) and mineralized (H) complex PPS structures. (I, J) SEM images of non-mineralized (I) and mineralized (J) complex PPS structures. (K) XPS analysis of the silicified sheets on Al foil at the

Figure 2. (*Continued.*) characteristic binding energies of 146 and 102 eV for electrons found in the 2s and 2p electron shells of the silicon atom, respectively. (L) ATR-FTIR spectroscopy of the silicified PPS; numbers indicate the peak wavenumbers (in 1095 cm^{-1}) of the Si–O–Si antisymmetric stretching modes. (M) Young's modulus of $_{R5}CsgA_{CBD}$/chitin PPS before and after silicification. $^{*}P < 0.05$, Student's *t* test. Note: the data were obtained by statistics from 256 × 256 spots in a 4 μm^2 square per sample.

Spectroscopy (FTIR) revealed peak wavenumbers at 1095 cm^{-1}, indicating that Si–O–Si antisymmetric stretching was occurring in the sheets (Fig. 2L). Highlighting the impressive mechanical properties of PPS after mineralization, we also used peak force quantitative nanomechanical (PK-QNM) AFM to measure the Young's modulus of non-mineralized and mineralized sheets and found that mineralization substantially increased the Young's modulus of the material by around 200% (from 4.84 ± 0.46 GPa to 14.16 ± 0.58 GPa) (Fig. 2M).

Collectively, by integrating rationally designed mineralization-promoting amyloid proteins with a microtransfer molding process, we precisely fabricated ordered porous structures that can be mineralized *in situ* across multiple scales, thereby resulting in hierarchically ordered mineralized structures resembling the exquisite frustules of diatoms [44]. These results implied that the $_{R5}CsgA_{CBD}$ fusion proteins can serve as self-assembling nanofibers that promote local silica mineralization. The SiO_2 mineral substantially enhances the mechanical properties of the free-standing PPS structures, thus potentially broadening a wide range of applications including serving as protective shelters for biomolecules and mechanical strengthening building materials [34]. For example, immobilization of enzymes in mechanically stable and chemically inert silica matrices would provide the embedded enzymes with better environmental tolerance and extended life-time storage, likely extending application of these biomolecules even under non-physiological conditions [25,46].

Biomimetic mineralization of $_{R5}CsgA_{CBD}$/chitin materials with TiO_2

Recalling the known ability of the R5 peptide to mediate the mineralization of TiO_2 [31], we next investigated whether the engineered $_{R5}CsgA_{CBD}$ amyloid nanofibers could nucleate metal oxide to generate mineralized nanostructures. The use of biomimetic mineralization approaches to produce porous metal oxide-based composites at room temperature is particularly attractive, given that metal oxide-based materials are known to be useful for a wide variety of applications in photocatalysis and photovoltaics [32].

We started to assess whether the engineered $_{R5}CsgA_{CBD}$ amyloid nanofibers could template the nucleation and growth of TiO_2. To such ends, we added nanofibers to buffered aqueous solutions containing Ti (IV) bis-(ammonium lactato)-dihydroxide (TiBALDH) to trigger TiO_2 mineralization. We found that the solutions became turbid when the $_{R5}CsgA_{CBD}$ nanofibers were added, implying their potential as self-assembling scaffolds to promote TiO_2 mineralization. We confirmed the successful mineralization of the R5-interacting TiO_2 using multiple analyses including EDS, selected area electron diffraction (SAED) and lattice fringe high-resolution transmission electron microscopy (HR-TEM). TEM and corresponding EDS analysis indicated the presence of Ti on the surface of the $_{R5}CsgA_{CBD}$ nanofibers exposed to the mineralization precursor solution and the presence of N (from the proteinaceous components) (Fig. 3A and B). Further, the SAED pattern obtained from the coatings close to the nanofiber surface revealed rings with spots having d-spacing of 3.5, 2.4 and 2.3 Å, corresponding to the lattice plane (101), (004) and (103), respectively (anatase phase, JCPDS 84–1286) (Fig. 3C). The relative intensities of the diffraction patterns matched the three most intense values for nanocrystalline TiO_2 (anatase phase, JCPDS 84–1286). Further, the lattice fringe spacings were consistent with the (101) plane spacing of anatase (anatase phase, JCPDS 84–1286) (Fig. 3D).

Having demonstrated successful mineralization at fibril level, we next assessed TiO_2 mineralization using the self-supporting porous sheets (Fig. 3E). After mineralization, we used nanoscale-infrared spectroscopy (nano-IR) at a wavenumber of 750 cm^{-1} to reveal the presence of TiO_2 on the mineralized sample, and indeed an overlay of the reconstituted topography image (3D) with a color code representing the absorption intensity at 750 cm^{-1} clearly indicated the homogeneous distribution of TiO_2 on the sheets (Fig. 3F and G). Moreover, corresponding chemical mapping analyses based on EDS further indicated the successful TiO_2 mineralization (Supplementary Fig. 10). In addition, XPS spectral analysis revealed that the mineralized sheets had distinct signals for oxygen (O 1s and 2s), carbon (C 1s), nitrogen (N 1s) and titanium (Ti 2p and 3p) (Fig. 3H), again supporting successful TiO_2 mineralization of the PPS. We next measured the Young's modulus to assess the effects of TiO_2 mineralization on the mechanical

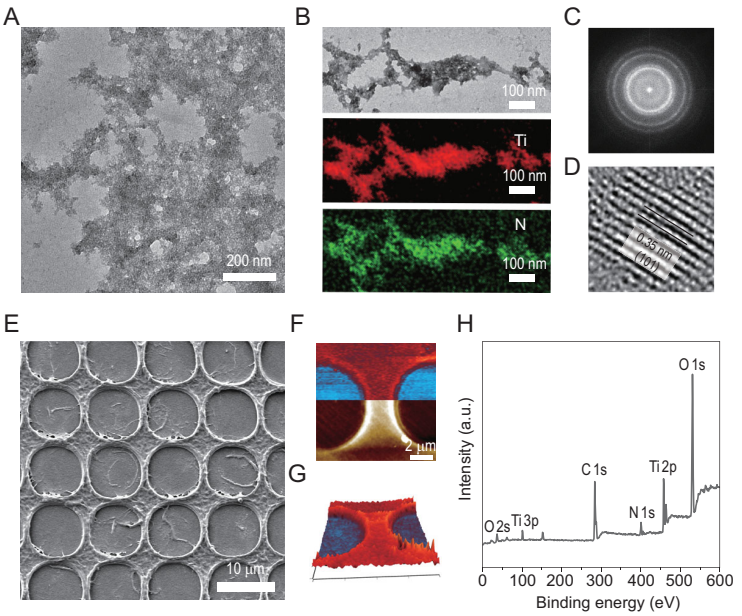

Figure 3. Biomimetic mineralization of TiO_2 with self-assembling $_{R5}CsgA_{CBD}$ nanofiber networks and self-supporting PPS. (A–C) Morphological, elemental and structural analysis of the mineralized $_{R5}CsgA_{CBD}$ nanofibers: (A) TEM image, (B) TEM-EDS images and (C) diffraction pattern. Note the diffraction ring representative of a typical anatase phase for TiO_2 mineral. (D) HR-TEM analysis of a microsphere fragment showing the (101) lattice fringes of the crystal. (E–H) Morphological and structural analysis of the mineralized PPS: (E) SEM image, (F) AFM topography (bottom) and IR absorption (top) images showing where mineralized TiO_2 (using Ti-O stretch absorption at 750 cm^{-1}) were localized on the sheets. (G) The 3D overlaid image combining topography and IR absorption showing the homogeneous and topographic distribution of TiO_2 on the patterned sheets. Note: red and blue colors indicate strong and weak Ti-O stretch absorption, respectively. (H) XPS survey spectra of TiO_2 mineralized $_{R5}CsgA_{CBD}$ PPS showing the chemical identity.

properties of PPS based on PK-QNM AFM methodology: the mineral indeed increased the elasticity of the PPS (from 4.84 ± 0.46 GPa to 7.21 ± 0.51 GPa) (Supplementary Fig. 11). Notably, using a similar biomimetic mineralization approach, Ga_2O_3, an ultra-wide bandgap oxide semiconductor, could also be mineralized on both nanofibers and porous $_{R5}CsgA_{CBD}$/chitin sheets (Supplementary Figs 12–14). Collectively, these results establish that porous $_{R5}CsgA_{CBD}$/chitin sheets can serve as scaffolds for templating the *in situ* growth of metal oxides to produce mineralized porous sheets over multiple length scales.

Fabrication of self-supporting and high surface area mineralized porous structures

The hierarchical porous structures of diatoms endow them with adaptive functions [5–7], providing inspiration for reconstructing artificial hierarchical porous materials for numerous applications. Previous studies have demonstrated that hierarchically structured porous bioceramic-silk composites could enhance cell attachment, proliferation and gene expression, and porous silica-based structures could facilitate enzyme immobilization, while porous organic polymers serve as a promising platform for designing heterogeneous catalysts [47–49]. Motivated by the applications of such diatom-inspired structures, we turned to construct porous mineralized $_{R5}CsgA_{CBD}$/chitin composites with high-surface areas and photo-reactivity for proof-of-concept demonstration of a solar-driven hydrogen evolution system.

To such ends, we started by preparing a 3D porous $_{R5}CsgA_{CBD}$-chitin complex scaffold for TiO_2 mineralization. We first applied HFIP ink containing both $_{R5}CsgA_{CBD}$ monomers and chitin, along with a porous sugar cube as a bulk template, to fabricate 3D complex self-supporting structures (Fig. 4A). After 12-h immersion in HFIP ink, the sugar cube was cured under methanol vapor to trigger the reassembly of amyloid proteins into nanofibers throughout the whole matrix of the cube. After dissolving the sugar cube template in aqueous solution, a self-supporting 3D amyloid-chitin complex structure was obtained. The successful replication of the sugar cube shape as a sponge-like structure was evident in normal photographs (Fig. 4B), and the porous surfaces of the scaffold were found to comprise a large amount of nanofiber structures under SEM (Fig. 4C and D). Notably, the air-dried 3D porous structures could spontaneously restore their shapes in their hydration state after immersion in different solutions (e.g. distilled water and Congo red solution) (Fig. 4E–H and Supplemental Fig. 15), and rapidly reached equilibrium swelling ratio in solution within 25 s (Fig. 4I). Additionally, these structures exhibited reversible hydration/dehydration behaviors with nearly identical swelling/de-swelling ratios even after multiple cycles (Fig. 4J), thus allowing for recyclable loading and release of specific reagents in a controlled manner.

With their rapid swelling feature and reversible swelling behavior, we hypothesize that the fabricated porous cubes would first serve as sponge-like materials to homogeneously absorb a mineralization precursor solution for TiO_2 mineralization, and then harbor a mixed reaction solution containing bacterial cells for artificial photosynthesis. Ideally, in the final constructed artificial photosynthesis system, mineralized TiO_2 nanoparticles would act as the light-antennae component converting photons into electrons, and an engineered *E. coli* strain harboring a hydrogenase gene cluster, upon receiving electrons transported by methyl viologen (MV), could catalyze continuous hydrogen evolution when the system was illuminated [50].

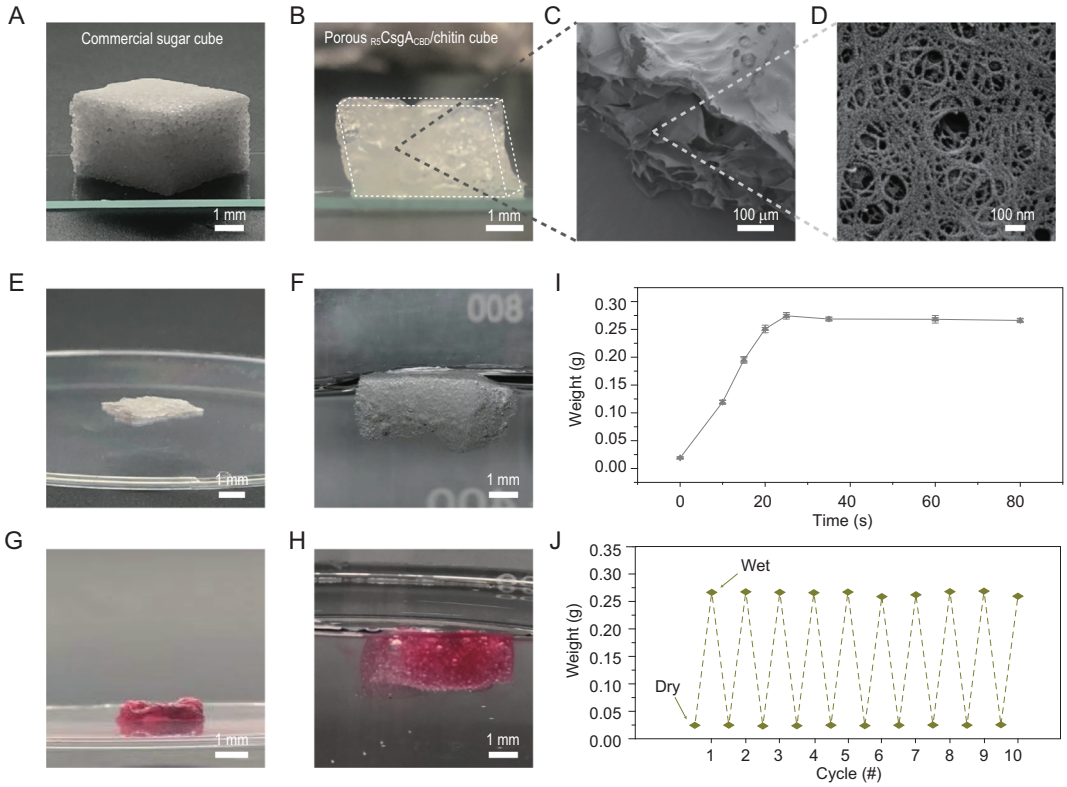

Figure 4. Morphological characterization and reversible dehydration/hydration behaviors of the fabricated porous $_{R5}$CsgA$_{CBD}$/chitin cube. (A, B) Digital photographs of the commercial sugar cube (A) and the fabricated porous $_{R5}$CsgA$_{CBD}$/chitin cube in initial hydration state (B). (C) SEM image showing the internal porous structures of the fabricated $_{R5}$CsgA$_{CBD/}$chitin cube. (D) SEM image of a zoomed-in area from (C), revealing that the cube is composed of nanofibers. (E–H) Digital camera snapshots of the same porous $_{R5}$CsgA$_{CBD}$/chitin cube switching between dehydration (dry) state and hydration state in different solutions: a dry sample (E) swells and floats at the surface of aqueous solution, resulting in swollen sponge (F); the dehydrated sample (G) from (H) re-swells into original sponge-like shape in Congo red solution. (I) Weight changes of the porous $_{R5}$CsgA$_{CBD}$/chitin cube as a function of swelling time in aqueous solution. Data are presented as mean ± SD ($n = 3$ repeats). (J) Weights of the same cube in hydration and dehydration state after multiple cycles of hydration/dehydration, illustrating the reversible hydration/dehydration behavior of the porous $_{R5}$CsgA$_{CBD}$/chitin cube. Note: To obtain completely dry samples, filter papers and constant N_2 blowing were applied to remove the trapped water in the hydrated samples.

We next probed whether the fabricated porous 3D cubes could promote local TiO_2 mineralization and whether the mineralized porous cubes could further absorb and harbor bacterial from aqueous solution (Fig. 5A and B). After 2-h incubation in a TiBALDH mineralization precursor solution, the 3D cube structures maintained their original shape (Fig. 5C). SEM and EDS analysis revealed that mineralized TiO_2 nanoparticles could directly form on the fibers comprising the cube (Fig. 5D and Supplemental Fig. 16). The UV-Vis absorption spectra showing a sharp absorption edge at ∼385 nm representative of TiO_2 bandgap excitation, further confirmed the successful mineralization of TiO_2 in the porous cube (Supplementary Fig. 17).

Nanoindentation measurements showed that the Young's modulus of the TiO_2-mineralized cube was obviously higher than that of the unmineralized cube (Supplementary Fig. 18), with values of 8.58 ± 1.63 GPa and 33.14 ± 6.58 GPa for the unmineralized and mineralized cube structures, respectively. In addition, after incubation of the mineralized cube in an aqueous solution containing the engineered *E. coli* strain, SEM analysis clearly indicated that the bacteria could distribute homogeneously inside the porous structure of the mineralized cube (Fig. 5E and F). These results therefore confirm that the 3D structures can serve as 3D scaffolds for biomimetic mineralization and for trapping bacterial cells.

Artificial photosynthesis of the photoreactive mineralized porous structures

Biogenic hydrogen production coupling microbials with protective shelters is a well-known technique in the field. In particular, *cyanobacteria* (e.g. *Synechocystis* sp., *Microcystis aeruginosa*, *Phormidium*

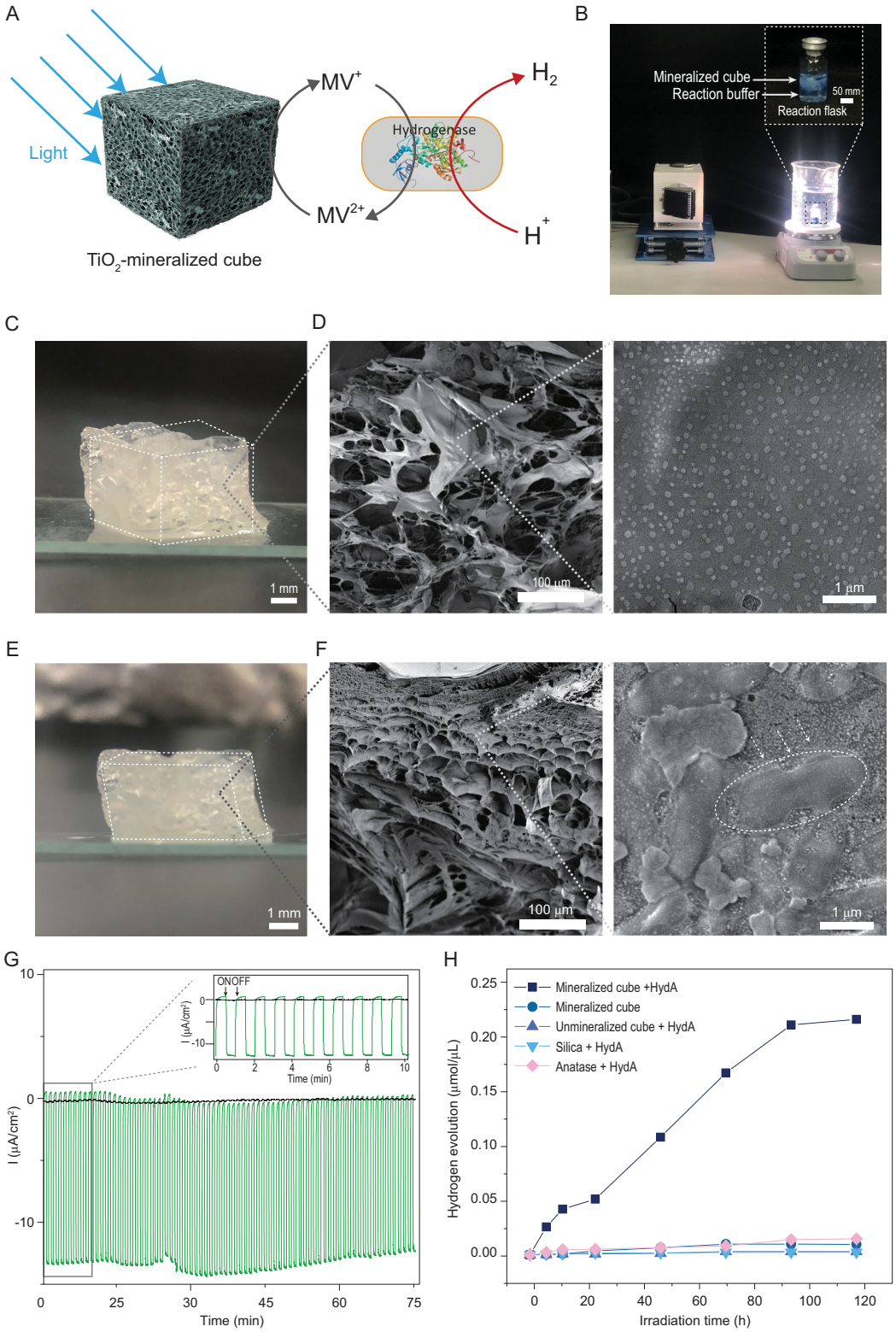

Figure 5. Bio-inspired construction of an artificial photosynthesis system for hydrogen evolution by coupling high surface area, self-supporting, 3-D porous mineralized cubes with colonized engineered *E. coli* cells. (A) Schematic illustration of an artificial photosynthesis system for H_2 evolution based on the mineralized $_{R5}CsgA_{CBD}$/chitin cubes, in which mineralized TiO_2 nanoparticles act as light-antennae for converting photons into electrons and engineered *E. coli* cells harboring a hydrogenase gene cluster are in close proximity to the TiO_2 structures, enabling constant hydrogen evolution upon receiving electrons delivered by methyl violet (MV). (B) Photograph image of hydrogen evolution equipment for the artificial

Figure 5. (*Continued.*) photosynthesis systems based on mineralized porous cube structures. (C, D) Morphologies of non-mineralized and mineralized porous $_{R5}CsgA_{CBD}$/chitin cubes before loading with engineered *E. coli* cells: (C) photograph images of mineralized porous $_{R5}CsgA_{CBD}$/chitin cubes; (D) SEM images of mineralized porous $_{R5}CsgA_{CBD}$/chitin cubes. (E, F) Morphologies of the mineralized porous $_{R5}CsgA_{CBD}$/chitin cubes after incubation with engineered *E. coli* cells: (E) photographic and (F) SEM images. (G) Transient photocurrents generated by mineralized TiO_2 $_{R5}CsgA_{CBD}$/chitin porous cubes. The green curve represents the photocurrent of the mineralized $_{R5}CsgA_{CBD}$/chitin cube structure deposited on FTO glass, when illuminated (on) or shielded (off) from visible light. The black curve represents the photocurrent of non-mineralized $_{R5}CsgA_{CBD}$-chitin materials on FTO glass. (H) H_2 evolution over time catalyzed with different hybrid systems: the mineralized cube reaction system (navy blue curve), the system utilizing excessive amount of free TiO_2 nanoparticles (pink curve), the cubic system lacking engineered strain (green curve), the cubic system containing the engineered strain but lacking mineralized TiO_2 (indigo curve) and the SiO_2 mineralized scaffolds containing engineered strain (light green curve). Note: The light source used here was a 300 W Xenon lamp (CEL-HXF300, CEAULIGHT) with illumination intensity of 20.07 mW/cm^2. A three-electrode system was used for photocurrent testing. A platinum wire and an Ag/AgCl were used as counter and reference electrodes, respectively. The applied potential was 0 V, and the electrolyte solution was 0.5 M Na_2SO_4. The solution was purged with continuous N_2 bubbles for 30 min to get rid of oxygen in the electrolyte cell. The experiments in G and H were replicated at least three times with identical results.

valderianum) have been used for hydrogen production via direct photolysis [51,52]. When encapsulated in a 1.5% agar matrix, the cyanobacteria *Oscillatoria* sp. showed that the rate and longevity of hydrogen production increased significantly compared to that of free cells [52]. The cyanobacteria *Synechocystis* sp. *PCC 6803* in silica matrices showed that hydrogen production of encapsulated cells was higher than that of cells in suspension [53,54]. Despite these advances, hydrogen production efficiency using biological organisms has been limited by its low volumetric productivity. As such, there has been interest in semi-artificial photosynthesis coupling inorganic semiconductor catalysts with engineered cells for their high performance in terms of broad-spectrum absorption and light harvesting efficiency [55].

We next explored the use of mineralized TiO_2 cubes in an artificial photosynthesis system for solar-driven hydrogen production. To such ends, we first measured the transient photocurrent of a mineralized amyloid cube by placing it onto a piece of FTO-conductive glass and dried the sample at 37°C overnight (Supplementary Fig. 19). The glass coated with the dried sample was then successfully used as an electrode: a transient photocurrent of 12.7 ± 1.1 μA/cm^2 was detected when it was exposed to light and the value dropped to almost zero when illumination was terminated, thus highlighting its pronounced property of photoresponse (Fig. 5G). Moreover, we tested the voltammetry responses of a bare FTO substrate and of TiO_2-mineralized cube deposited on the FTO electrode in 0.50 M aqueous Na_2SO_4 (pH = 6.3). No redox peak was observed for both mineralized TiO_2 and bare FTO glass over a wide voltage range of $-0.1 \sim 1.4$ V vs RHE, and the curves of their cyclic voltammetry are identical, implying the electrochemical stability of the TiO_2-mineralized cube under aqueous conditions (Supplementary Fig. 20).

With this photocatalytic mineralized cube reaction system established, we next carried out H_2 evolution in the aforementioned semi-solid artificial photosynthetic system comprising a bacterial strain that expresses a hydrogenase (and its required maturases), TEOA as the sacrificial agent and MV as the mediator. UV spectroscopy revealed peaks between 300–400 nm and 500–700 nm, confirming the $MV^{+\cdot}$ formation upon illumination (but not under dark conditions) (Supplementary Fig. 21) [56]. We first assessed how the reaction system performed in terms of hydrogen production under different conditions. As revealed, a final H_2 concentration of 0.21 μmol/μL was obtained after 120 h reaction based on the mineralized cube reaction system (navy blue curve), which was substantially higher than that of the system using the excessive amount of free TiO_2 nanoparticles (0.014 μmol/μL) (pink curve). In contrast, almost no H_2 evolution was found for the cubic system lacking engineered strain (green curve), and for the cubic system containing the engineered strain but lacking mineralized TiO_2 (indigo curve). Meanwhile, H_2 production was not detected in the SiO_2-mineralized scaffolds containing engineered strain (light green curve) (Fig. 5H). Based on the results, we determined the optimized conditions for our semi-artificial cubic system: the initial cell density applied is around 1×10^9 colony forming units (cfu) and solution pH = 8. (Supplementary Fig. 22). Conceivably, the 3D porous cube provides an ideal confined space in which mineralized TiO_2 and engineered bacterial are in good contact with each other, ensuring high-efficiency solar-driven hydrogen evolution. In addition, the results indicated that the hydrogen production efficiency of a biological enzymatic system could be substantially enhanced when combined with mineralized TiO_2. We envision that our 3D porous mineralized material systems coupled with colonized engineered bacteria may serve as a

viable alternative route for conducting various artificial photosynthetic reactions.

CONCLUSION

Diatom frustules represent exquisite masterpiece examples of natural hierarchical composite materials, generating keen interest for exploring various diatom-inspired scaffolds for biomimetic mineralization. Despite important advances, it is still challenging to fully recapitulate the multiscale mineralization features and functions of natural diatom structures in current state-of-the-art biomimetic composites. In our view, the difficulties of biomimetic mineralization research to reconstruct the spectacular morphologies and their remarkable material properties of natural composite materials arise, at least in part, from the inability to precisely order the molecular recognition and interactions at the organic–inorganic interfaces (e.g. closely mimicking the polysaccharide–protein–mineral interactions) across multiple scales with existing bio-derived or bio-inspired scaffolds. Our self-supporting PPS and porous sponge-like architectures, made of genetically programmable amyloid proteins and polysaccharide chitin, for biomimetic multiscale mineralization have thus brought us a step closer to nature. As demonstrated, the produced 3D architectures can template the formation of diverse minerals across multiple length scales, and the resultant mineralized porous composites can be further used for performing solar-driven hydrogen evolution reactions, opening the door for exploiting porous mineralized structures for various artificial photosynthesis systems. Additionally, our studies will spur new interest in designing sophisticated 3D scaffolds for multiscale mineralization by rationally incorporating the hidden molecular recognitions among protein–polysaccharide–mineral interfaces of natural minerals through genetic engineering.

Moving forward, given the genetically engineerable aspect of our mineralization scaffolds, it should be quite straightforward to develop additional biomimetic mineralization fusion proteins by swapping the silica-nucleating R5 peptide for other peptides that are known to mediate the mineralization of inorganic nanomaterials, thereby substantially expanding the versatility and applications of this general biomimetic mineralization design strategy. For example, porous CoPt catalytic materials should be easily generated based on a cobalt-binding peptide Co1-P10 that can control the nucleation of CoPt nanoparticles, while porous hydroxyapatite (HA) composites can be fabricated by applying fusion proteins containing HA-promoting protein domains found in bone.

STATISTICS

Data analysis was performed on Origin 2019b software and presented as mean ± SD (standard deviation), calculated based on at least three replicates. Statistical comparisons between two groups were based on Student's *t* test with two tailed distribution, and *P*-values less than 0.05 were considered to be statistically significant.

SUPPLEMENTARY DATA

Supplementary data are available at *NSR* online.

ACKNOWLEDGEMENTS

We thank Xinyan Wang of the Analytical Instrumentation Center at the School of Physical Science and Technology of ShanghaiTech University, as well as Qing Zhang, Haiyin Zhu, Weiyan Liu, Yilan Jiang and Yujuan Zhao of the Center for High-resolution Electron Microscopy of ShanghaiTech University for providing technical support and assistance in data collection and analysis.

FUNDING

This work was partially supported by the Key Program of the National Natural Science Foundation of China (U1932204), the Science and Technology Commission of Shanghai Municipality (17JC1403900) and the China Postdoctoral Science Foundation (2019M661665).

AUTHOR CONTRIBUTIONS

C.Z. conceived the concept and directed the research. C.Z., K.L. and Y.L. conceived the technical details, designed the experiments and analyzed the data. M.C. assisted in performing the mechanical tests. B.A. participated in the construction of the plasmid. X.W. and H.P. participated in experiments in building up the artificial photosynthesis system. J.L., B.Z. and G.M. assisted in measuring the H_2 production by gas chromatography.

Conflict of interest statement. The authors have applied for a provisional patent based on this work with the China Intellectual Property Office (PCT/CN2018/085988).

REFERENCES

1. Li A, Zhang W and Ghaffarivardavagh R *et al.* Towards uniformly oriented diatom frustule monolayers: experimental and theoretical analyses. *Microsyst Nanoeng* 2016; **2**: 16064.
2. Losic D, Mitchell JG and Voelcker NH. Diatomaceous lessons in nanotechnology and advanced materials. *Adv Mater* 2009; **21**: 2947–58.
3. Gutierrez A, Guney MG and Fedder GK *et al.* The role of hierarchical design and morphology in the mechanical response of diatom-inspired structures via simulation. *Biomater Sci* 2017; **6**: 146–53.

4. Hamm CE, Merkel R and Springer O *et al.* Architecture and material properties of diatom shells provide effective mechanical protection. *Nature* 2003; **421**: 841–3.
5. Romann J, Valmalette JC and Royset A *et al.* Optical properties of single diatom frustules revealed by confocal microspectroscopy. *Opt Lett* 2015; **40**: 740–3.
6. Jeffryes C, Solanki R and Rangineni Y *et al.* Electroluminescence and photoluminescence from nanostructured diatom frustules containing metabolically inserted germanium. *Adv Mater* 2008; **20**: 2633–7.
7. Gale DK, Gutu T and Jiao J *et al.* Photoluminescence detection of biomolecules by antibody-functionalized diatom biosilica. *Adv Funct Mater* 2009; **19**: 926–33.
8. Bagshaw SA, Prouzet E and Pinnavaia TJ. Templating of mesoporous molecular sieves by nonionic polyethylene oxide surfactants. *Science* 1995; **269**: 1242–4.
9. Han W, MacEwan SR and Chilkoti A *et al.* Bio-inspired synthesis of hybrid silica nanoparticles templated from elastin-like polypeptide micelles. *Nanoscale* 2015; **7**: 12038–44.
10. Hossain K-Z and Sayari A. Synthesis of onion-like mesoporous silica from sodium silicate in the presence of α,ω-diamine surfactant. *Microporous Mesoporous Mater* 2008; **114**: 387–94.
11. Zimny K, Blin JL and Stebe MJ. Ordered mesoporous silica templated by nonionic fluorinated liquid crystals. *J Phys Chem C* 2009; **113**: 11285–93.
12. Cervantes-Martinez CV, Emo M and Garcia-Celma MJ *et al.* Morphosynthesis of porous silica from biocompatible templates. *Chem Eng Res Des* 2019; **151**: 179–89.
13. Kresge CT, Leonowicz ME and Roth WJ *et al.* Ordered mesoporous molecular sieves synthesized by a liquid-crystal template mechanism. *Nature* 1992; **359**: 710–2.
14. Kamalov M, Hajradini A and Rentenberger C *et al.* N-terminal residues of silaffin peptides impact morphology of biomimetic silica particles. *Mater Lett* 2018; **212**: 114–7.
15. Kroger N, Deutzmann R and Sumper M. Polycationic peptides from diatom biosilica that direct silica nanosphere formation. *Science* 1999; **286**: 1129–32.
16. Belegratis MR, Schmidt V and Nees D *et al.* Diatom-inspired templates for 3D replication: natural diatoms versus laser written artificial diatoms. *Bioinspir Biomim* 2014; **9**: 016004.
17. Briggs BD and Knecht MR. Nanotechnology meets biology: peptide-based methods for the fabrication of functional materials. *J Phys Chem Lett* 2012; **3**: 405–18.
18. Brott LL, Naik RR and Pikas DJ *et al.* Ultrafast holographic nanopatterning of biocatalytically formed silica. *Nature* 2001; **413**: 291–3.
19. Canabady-Rochelle LL, Belton DJ and Deschaume O *et al.* Bioinspired silicification of silica-binding peptide-silk protein chimeras: comparison of chemically and genetically produced proteins. *Biomacromolecules* 2012; **13**: 683–90.
20. Jin RH, Yao DD and Levi RT. Biomimetic synthesis of shaped and chiral silica entities templated by organic objective materials. *Chemistry* 2014; **20**: 7196–214.
21. Jin RH and Yuan JJ. Shaped silicas transcribed from aggregates of four-armed star polyethyleneimine with a benzene core. *Chem Mater* 2006; **18**: 3390–6.
22. Jung JH, Yoshida K and Shimizu T. Creation of novel double-helical silica nanotubes using binary gel system. *Langmuir* 2002; **18**: 8724–7.
23. Sugiyasu K, Tamaru S and Takeuchi M *et al.* Double helical silica fibrils by sol-gel transcription of chiral aggregates of gemini surfactants. *Chem Commun* 2002; **11**: 1212–3.
24. Lechner CC and Becker CF. Silaffins in silica biomineralization and biomimetic silica precipitation. *Mar Drugs* 2015; **13**: 5297–333.
25. Chrzanowska A and Derylo-Marczewska A. Mesoporous silica/protein biocomposites: surface, topography, thermal properties. *Int J Biol Macromol* 2019; **139**: 531–42.
26. Pipattanawarothai A, Suksai C and Srisook K *et al.* Non-cytotoxic hybrid bioscaffolds of chitosan-silica: sol-gel synthesis, characterization and proposed application. *Carbohydr Polym* 2017; **178**: 190–9.
27. Shchipunov YA and Karpenko TY. Hybrid polysaccharide-silica nanocomposites prepared by the sol-gel technique. *Langmuir* 2004; **20**: 3882–7.
28. Singh V, Srivastava P and Singh A *et al.* Polysaccharide-silica hybrids: design and applications. *Polym Rev* 2016; **56**: 113–36.
29. Spinde K, Kammer M and Freyer K *et al.* Biomimetic silicification of fibrous chitin from diatoms. *Chem Mater* 2011; **23**: 2973–8.
30. Wysokowski M, Behm T and Born R *et al.* Preparation of chitin-silica composites by in vitro silicification of two-dimensional lanthella basta demosponge chitinous scaffolds under modified Stober conditions. *Mater Sci Eng C Mater Biol Appl* 2013; **33**: 3935–41.
31. Sewell SL and Wright DW. Biomimetic synthesis of titanium dioxide utilizing the R5 peptide derived from *Cylindrotheca fusiformis*. *Chem Mater* 2006; **18**: 3108–13.
32. Sumerel JL, Yang WJ and Kisailus D *et al.* Biocatalytically templated synthesis of titanium dioxide. *Chem Mater* 2003; **15**: 4804–9.
33. Kisailus D, Choi JH and Weaver JC *et al.* Enzymatic synthesis and nanostructural control of gallium oxide at low temperature. *Adv Mater* 2005; **17**: 314–8.
34. Liu X, Zhang F and Jing X *et al.* Complex silica composite nanomaterials templated with DNA origami. *Nature* 2018; **559**: 593–8.
35. Guo J, Ling SJ and Li WY *et al.* Coding cell micropatterns through peptide inkjet printing for arbitrary biomineralized architectures. *Adv Funct Mater* 2018; **28**: 1800228.
36. Zhong C, Gurry T and Cheng AA *et al.* Strong underwater adhesives made by self-assembling multi-protein nanofibres. *Nat Nanotechnol* 2014; **9**: 858–66.
37. Li Y, Li K and Wang X *et al.* Patterned amyloid materials integrating robustness and genetically programmable functionality. *Nano Lett* 2019; **19**: 8399–408.
38. Ikegami T, Okada T and Hashimoto M *et al.* Solution structure of the chitin-binding domain of Bacillus circulans WL-12 chitinase A1. *J Biol Chem* 2000; **275**: 13654–61.
39. Knecht MR and Wright DW. Functional analysis of the biomimetic silica precipitating activity of the R5 peptide from *Cylindrotheca fusiformis*. *Chem Commun* 2003; **24**: 3038–9.
40. Kroger N, Lorenz S and Brunner E *et al.* Self-assembly of highly phosphorylated silaffins and their function in biosilica morphogenesis. *Science* 2002; **298**: 584–6.
41. Lechner CC and Becker CF. A sequence-function analysis of the silica precipitating silaffin R5 peptide. *J Pept Sci* 2014; **20**: 152–8.
42. Brunner E, Richthammer P and Ehrlich H *et al.* Chitin-based organic networks: an integral part of cell wall biosilica in the diatom Thalassiosira pseudonana. *Angew Chem Int Ed Engl* 2009; **48**: 9724–7.
43. Cui M, Qi Q and Gurry T *et al.* Modular genetic design of multi-domain functional amyloids: insights into self-assembly and functional properties. *Chem Sci* 2019; **10**: 4004–14.
44. Qin D, Xia Y and Whitesides GM. Soft lithography for micro- and nanoscale patterning. *Nat Protoc* 2010; **5**: 491–502.
45. Senior L, Crump MP and Williams C *et al.* Structure and function of the silicifying peptide R5. *J Mater Chem B* 2015; **3**: 2607–14.
46. Albert K, Huang XC and Hsu HY. Bio-templated silica composites for next-generation biomedical applications. *Adv Colloid Interface Sci* 2017; **249**: 272–89.

47. Parlett CM, Wilson K and Lee AF. Hierarchical porous materials: catalytic applications. *Chem Soc Rev* 2013; **42**: 3876–93.
48. Sun MH, Huang SZ and Chen LH *et al.* Applications of hierarchically structured porous materials from energy storage and conversion, catalysis, photocatalysis, adsorption, separation, and sensing to biomedicine. *Chem Soc Rev* 2016; **45**: 3479–563.
49. Yang XY, Chen LH and Li Y *et al.* Hierarchically porous materials: synthesis strategies and structure design. *Chem Soc Rev* 2017; **46**: 481–558.
50. Wang XY, Pu JH and Liu Y *et al.* Immobilization of functional nano-objects in living engineered bacterial biofilms for catalytic applications. *Natl Sci Rev* 2019; **6**: 929–43.
51. Saper G, Kallmann D and Conzuelo F *et al.* Live cyanobacteria produce photocurrent and hydrogen using both the respiratory and photosynthetic systems. *Nat Commun* 2018; **9**: 2168.
52. Léonard A, Rooke JC and Meunier CF *et al.* Cyanobacteria immobilised in porous silica gels: exploring biocompatible synthesis routes for the development of photobioreactors. *Energy Environ Sci* 2010; **3**: 370–7.
53. Touloupakis E, Rontogiannis G and Benavides AMS *et al.* Hydrogen production by immobilized *Synechocystis* sp. PCC 6803. *Int J Hydrog Energy* 2016; **41**: 15181–6.
54. Leonard A, Dandoy P and Danloy E *et al.* Whole-cell based hybrid materials for green energy production, environmental remediation and smart cell-therapy. *Chem Soc Rev* 2011; **40**: 860–85.
55. Wang B, Zeng C and Chu KH *et al.* Enhanced biological hydrogen production from escherichia coli with surface precipitated cadmium sulfide nanoparticles. *Adv Energy Mater* 2017; **7**: 1700611.
56. King PW, Posewitz MC and Ghirardi ML *et al.* Functional studies of [FeFe] hydrogenase maturation in an *Escherichia coli* biosynthetic system. *J Bacteriol* 2006; **188**: 2163–72.